Atomistic description of self-diffusion in molybdenum: A comparative theoretical study of non-Arrhenius behavior

Daria Smirnova,[1,*] Sergei Starikov,[1] Grisell Díaz Leines,[1] Yanyan Liang,[1] Ning Wang,[1] Maxim N. Popov,[2] Igor A. Abrikosov,[3] Davide G. Sangiovanni,[1,3] Ralf Drautz,[1] and Matous Mrovec[1]

[1]*The Interdisciplinary Centre for Advanced Materials Simulation (ICAMS), Ruhr-Universität Bochum, Germany*

[2]*Materials Center Leoben Forschung GmbH, Leoben, Austria*

[3]*Department of Physics, Chemistry and Biology (IFM), Linköping University, SE-581 83 Linköping, Sweden*

(Received 14 August 2019; published 14 January 2020)

According to experimental observations, the temperature dependence of self-diffusion coefficient in most body-centered cubic metals (bcc) exhibits non-Arrhenius behavior. The origin of this behavior is likely related to anharmonic vibrational effects at elevated temperatures. However, it is still debated whether anharmonicity affects more the formation or migration of monovacancies, which are known to govern the self-diffusion. In this extensive atomistic simulation study we investigated thermodynamic properties of monovacancies in bcc molybdenum, here taken as a representative model system, from zero temperature to the melting point. We combined first-principles calculations and classical simulations based on three widely used interatomic potentials for Mo. In our analysis we employ static and dynamic atomistic calculations as well as statistical sampling techniques and thermodynamic integration to achieve thorough information about temperature variations of vacancy formation and migration free energies and diffusivities. In addition, we carry out large-scale molecular dynamics simulations that enable direct observation of high-temperature self-diffusion at the atomic scale. By scrutinizing the results obtained by different models and methods, we conclude that the peculiar self-diffusion behavior is likely caused by strong temperature dependence of the vacancy formation energy.

DOI: 10.1103/PhysRevMaterials.4.013605

I. INTRODUCTION

Self-diffusion via vacancy migration belongs to fundamental transport mechanisms in most metals and alloys. Even though this phenomenon has been studied extensively both experimentally and theoretically (for reviews see, e.g., Refs. [1–8]), theoretical predictions of diffusion behavior still belong to very active areas of materials research. In particular, the interpretation of experimental observations and the consistency between experimental data and theoretical predictions have attracted great attention in recent years [8–16].

The self-diffusion coefficient, D_{self}, can be expressed in general as a product of the vacancy concentration, c_{vac}, and the single-vacancy diffusivity, D_{vac}, which depend on energies and entropies associated with vacancy formation and vacancy migration, respectively. These fundamental thermodynamic properties can nowadays be determined with high accuracy for $T = 0$ K by first-principles electronic structure methods based on density functional theory (DFT). The obtained values are generally consistent, although the influence of the employed exchange-correlation functionals can be significant [8,17–20]. What remains challenging for *ab initio* methods is the description of diffusion at finite temperatures. Recent studies [10,13,14,19,21,22] have confirmed that the aforementioned vacancy energies/entropies are not necessarily constant but may vary with temperature, an assumption that has been suggested by various authors in the past [23–27].

Finite-temperature effects have usually been considered in electronic structure calculations via the quasiharmonic approximation. Nevertheless, it has been demonstrated recently [13,14] that anharmonic vibrational effects contribute significantly to the vacancy formation energy at elevated temperatures and need to be taken into account to obtain quantitative agreement with experimental data. However, an accurate evaluation of the anharmonic contributions is computationally very demanding and practically accessible only by combining DFT calculations with efficient configurational sampling and thermodynamic integration [28]. A direct evaluation of free energies by DFT is prohibitive due to the high computational cost of electronic structure calculations.

This limitation is much less severe for classical interatomic potentials that can nowadays be employed in molecular dynamics (MD) simulations of many thousands of atoms and simulation times exceeding several nanoseconds. Such times and system sizes are sufficient to follow diffusion processes at elevated temperatures and to obtain a direct comparison between theory and experiment. However, a well-known drawback of classical interatomic potentials is their limited transferability as well as the inability to explicitly capture phenomena that result from the electronic interactions (e.g., electronic entropy, magnetism). Despite these limitations, simulations with classical potentials can yield valuable insights into dynamical aspects of diffusion. They can therefore complement the findings of electronic structure calculations

*daria.smirnova@icams.rub.de

and reveal processes that are not directly accessible by DFT. In addition, large-scale MD simulations following the dynamical behavior of defects at elevated temperatures can serve for validation of interatomic potentials in extensive regions of configurational space.

The temperature dependence of diffusion coefficients in metals depends strongly on their cohesive properties as well as crystal structure. While face-centered cubic (fcc) metals exhibit only slightly upward curvature in the Arrhenius description of self-diffusion coefficients, [1,23] the diffusion behavior of body-centered cubic (bcc) metals shows much more pronounced variations. Not only the diffusivities in different bcc metals vary by several orders of magnitude at identical homologous temperatures, but the self-diffusion in most bcc metals does not follow the Arrhenius behavior and increases at high temperature [24–26,29–31]. This trend is most pronounced in the so-called anomalous bcc metals, such as Ti, Zr, U, and Hf, which undergo a phase transformation to the bcc structure only at elevated temperatures. In the case of bcc Mo, experimentally determined self-diffusion coefficients exhibit less strong but evident non-Arrhenius behavior [32] with positive curvature and enhanced diffusion at temperatures above 2000 K.

Several possible origins of the unusual self-diffusion in bcc metals have been proposed, including additional transport via self-interstitials or divacancies [24,30,33,34], temperature dependence of the vacancy migration energy [25,35,36], and temperature dependence of the vacancy formation energy [19,23]. A significant contribution of divacancies to the self-diffusion, which was the most widely accepted explanation for the enhanced diffusivity at high temperatures in the past, is now considered implausible [26,37–39]. Recent atomistic simulations [15,16,40,41] have revealed that self-interstitials can strongly enhance the self-diffusion but only in the anomalous bcc metals (e.g., Zr, Ti, U). Hence, the most likely reason responsible for the observed non-Arrhenius diffusion are the temperature variations of the vacancy formation and migration energies (E^f_{vac} and E^m_{vac}). However, it is not clear whether just one of them dominates or both of contribute similarly.

The *ab initio* molecular dynamics (AIMD) simulations of Mattsson *et al.* [19] showed that self-diffusion in Mo is associated with a marked temperature dependence of vacancy formation energy, in accordance with other DFT studies for fcc metals [9,10,13,14,28]. Later, Sangiovanni *et al.* [42] investigated vacancy jump rates in Mo using an accelerated nonequilibrium AIMD which enabled to extend the investigated temperature range down to 1000 K. Both studies employed a surface-corrected AM05 exchange-correlation functional that overestimates the vacancy formation energy [13,14]. In addition, the convergence of vacancy formation energies at finite temperatures using MD requires extensive simulation times that are not achievable by AIMD calculations [13].

Atomistic simulations that employ classical interatomic potentials present a powerful tool for the investigation of point defect properties at finite temperature. Several studies have been performed for fcc metals [10,21,43–45] where non-Arrhenius behavior is much less pronounced in comparison with bcc metals. For instance, Carling *et al.* [10] found that the slightly enhanced diffusion in Al at high temperature is induced by temperature dependence of the vacancy formation energy. The energy variation upon heating up to the melting temperature amounted to only about 10%; a change that is close to uncertainties of calculations as well as measurements. For bcc metals, previous classical MD studies focused mostly on the diffusion of a single vacancy, without detailed investigation of vacancy concentration [40,46–48]. More comprehensive investigations of self-diffusion were performed only for the bcc phases of Zr [16,49], U [15,41], and Fe [22,50]. However, as already mentioned, the primary origin of non-Arrhenius behavior in these metals are likely due to self-interstitials [16,51] or, in the case of Fe, magnetic excitations [52,53].

The main uncertainty in all classical calculations stems from the limited reliability and transferability of the interatomic potentials. Even though close attention is usually paid to fitting of equilibrium bulk (e.g., cohesive, elastic and vibrational properties) and defect properties (e.g., defect formation and migration energies) at 0 K, there is no *a priori* guarantee that the potentials will be able to capture correctly also dynamical behavior of defects at elevated temperatures. It is therefore important to assess the quantitative predictive accuracy of interatomic potentials especially for complex phenomena such as diffusion, which is affected by relatively subtle variations resulting from collective behavior of many atoms away from equilibrium.

In this work, we carry out a comprehensive analysis of self-diffusion in the bcc transition metal molybdenum using several classical interatomic potentials. We employ not only distinct interatomic models but combine also various methodologies to obtain detailed information about thermodynamic quantities governing diffusion and, in particular, to investigate the role of anharmonicity in the temperature dependencies of both the formation and migration energies and entropies. The predictions of the classical potentials are compared to experimental data as well as DFT results and hence provide a thorough information about the reliability of the models beyond the usual set of benchmark properties [54]. By using several interatomic potentials we obtain additional insights into features of each model that may be crucial for the correct prediction of diffusion. Our study relies predominantly on classical MD simulations, but we also exploit complementary statistical methodologies such as transition path sampling [55] and thermodynamic integration to achieve thorough information about temperature variations of vacancy formation and migration free energies and diffusivities.

The paper is organized as follows. In Sec. II, we provide a brief description of the atomistic models and methodologies used in this work and investigate fundamental material properties related to self-diffusion. Section III is devoted to in-depth analysis of finite-temperature properties of vacancies. Section IV presents results of large-scale molecular dynamics simulations of self-diffusion. Finally, in Sec. V, we analyze the results and present the main conclusions of our work.

II. COMPUTATIONAL MODELS AND METHODOLOGIES

There exist a number of interatomic potentials for atomistic simulations of pure molybdenum [48,54,56–64] and

TABLE I. Fundamental properties of bcc Mo predicted by the FS [56,57], MEAM [63], and ADP [15] interatomic potentials together with reference DFT and experimental values (the listed properties include lattice parameter at zero temperature a_0 in Å, cohesive energy E_{coh} in eV/atom, elastic constants C_{ij} in GPa, melting temperature T_m in K).

	Exp.	DFT	FS	MEAM	ADP
a_0	3.147[a]	3.163	3.147	3.167	3.1489
E_{coh}	6.82[b]	–	6.82	6.82	6.88
C_{11}	477[c]	483	465	425	548
C_{12}	155[c]	150	162	145	168
C_{44}	111[c]	109	109	96	160
T_m	2890[d]	–	2850	3220	2770

[a]Reference [76].
[b]Reference [77].
[c]Reference [78].
[d]Reference [79].

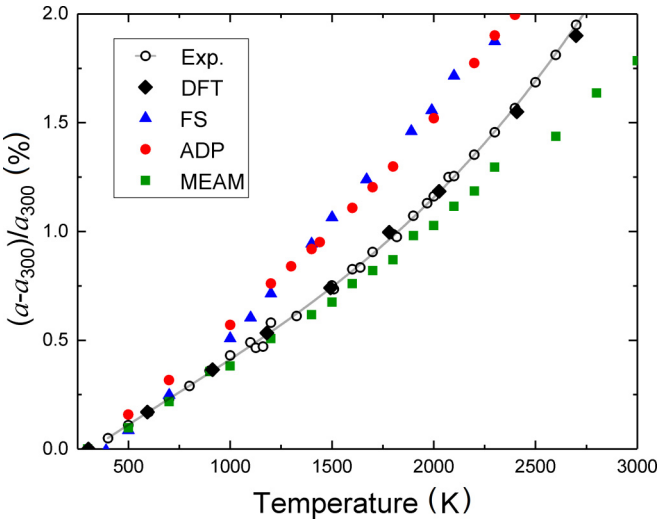

FIG. 1. Dependence of the lattice parameter on temperature predicted by three interatomic potentials and DFT calculations; reference experimental data are taken from Refs. [76,85,86] (the line is to guide the eye).

molybdenum-containing alloys [15,65–68]. For the purpose of this work, we choose three representative many-body potentials that reproduce not only fundamental properties of bulk bcc Mo but also capture the formation and migration energies of monovacancy well (see below).

The interatomic potentials employed in the study are:

(1) The Finnis and Sinclair (FS) potential [56], updated by Ackland and Thetford [57].

(2) The modified embedded-atom method (MEAM) potential constructed by Park *et al.* [63].

(3) The angular-dependent potential (ADP) developed by Starikov *et al.* [15].

The FS potential stems from the second-moment approximation of the electronic density of states [69]. The MEAM and ADP potentials are based on the embedded-atom method [70] with additional terms designed to describe angular interactions between atoms [71,72].

All classical simulations reported in this work were carried out using the LAMMPS code [73]. The size of the simulation blocks varied depending on the simulated property and is specified below. A time step between 0.5 and 1.0 fs was chosen for most MD simulations. As described in detail below, various statistical ensembles including the microcanonical NVE, canonical NVT, and isothermal-isobaric NPT ensembles were employed. The Nose-Hoover thermostat and barostat were used to control the temperature and pressure.

First-principles DFT computations were carried out using the VASP code [74]. We used projector augmented wave (PAW) method and the exchange-correlation functional within the generalized-gradient approximation (GGA) in the form of Perdew-Burke-Ernzerhof [75]. The Brillouin zone was sampled using a 5×5×5 Monkhorst-Pack **k**-point mesh. The cutoff energy of the plane-wave basis set was 500 eV. Unless noted otherwise, the DFT simulation supercells contained 128 Mo atoms.

A. Elastic properties, melting and thermal expansion

Table I summarizes several fundamental properties predicted by the three potentials together with reference experimental and DFT data. These properties are commonly used either as target or benchmark quantities during potential construction. For example, the FS potential was fitted to reproduce accurately the experimental lattice constant and elastic moduli. In the case of MEAM, the fitting was based on a combination of *ab initio* computed elastic constants, energies and interatomic forces. For ADP, the properties listed in Table I were not explicitly included in the fitting database. Instead, the ADP parametrization was fitted based on energies, forces and stress components obtained from DFT calculations for a number (typically about 100) diverse atomic configurations [80–82].

For consistency, all values of T_m given in Table I were computed in this work. The melting simulations were carried out by heating a 6 nm thick bcc slab containing two free (100) surfaces. The temperature was gradually increased from 2500 to 3500 K with a heating rate of 0.5 K/ps. The simulated system contained 5760 atoms with periodic boundary conditions along two directions parallel to the free surfaces. Initially, the atoms were arranged in the bcc lattice with lattice parameter corresponding to zero pressure at $T = 2500$ K. Simulations using the MEAM potential were performed with an initial lattice parameter corresponding to zero pressure at $T = 3000$ K due to a higher melting point predicted by this potential. The simulation conditions guarantee small stresses in the simulation block (less than 1 GPa) and accurate determination of T_m (within ∼10 K) [83]. For the FS potential, we obtained a value of T_m about 200 K lower than ∼3060 K obtained in Ref. [84] based on thermodynamic integration. For the MEAM and ADP potentials, our results agree closely with the original references [15,63].

Figure 1 shows the thermal expansion of bcc Mo. For reference, we compiled experimental data across various temperature ranges [76,85,86]. The figure also contains results of *ab initio* molecular dynamics simulations performed in this work. The AIMD runs were performed using the *NPT*

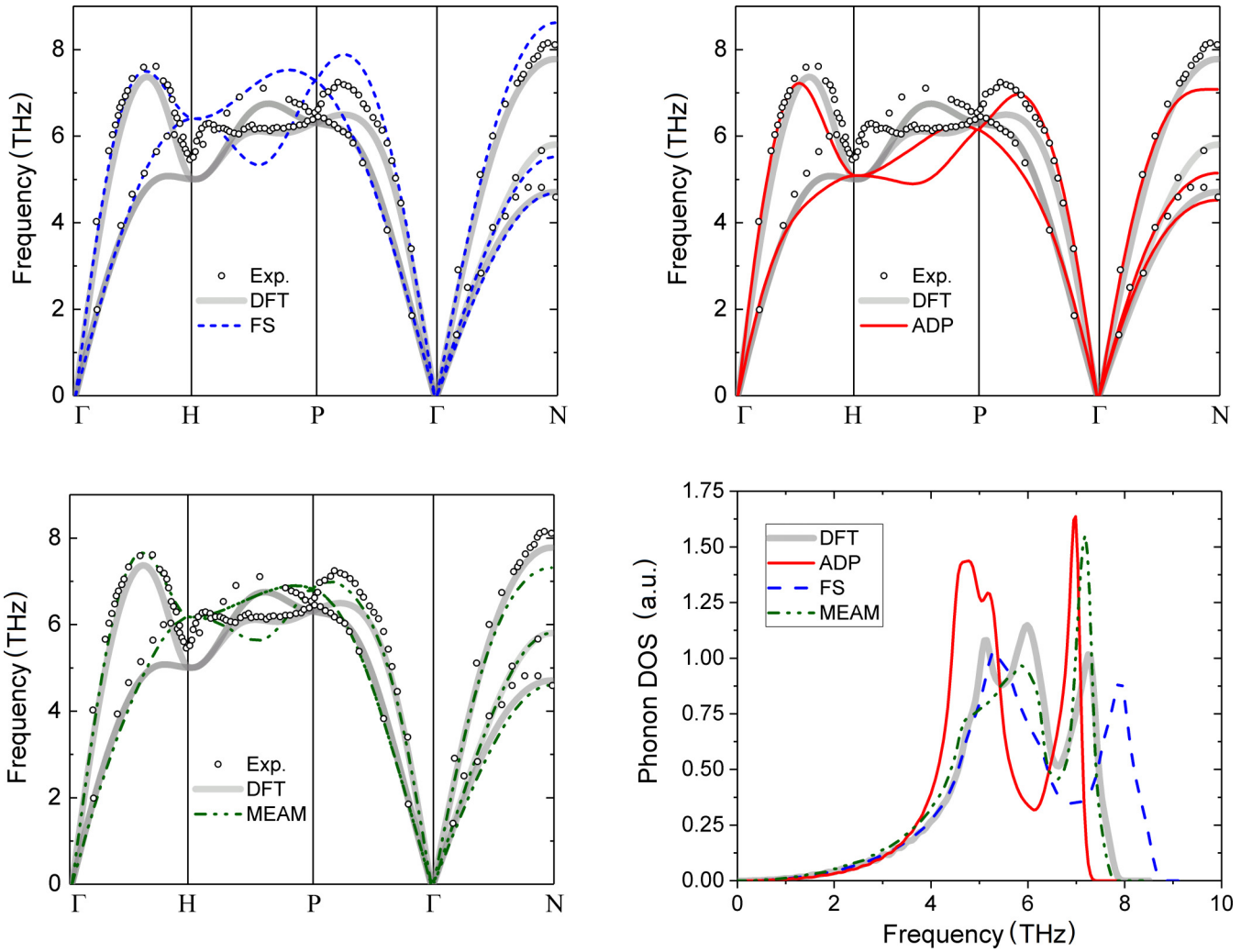

FIG. 2. A comparison of phonon-dispersion curves and phonon DOS curves for bcc Mo computed using three interatomic potentials employed in this work. Experimental data are taken from Ref. [88], DFT results from Ref. [54].

ensemble at different temperatures and zero pressure. Here we used Γ-point sampling, and a reduced plane-wave energy cutoff of 300 eV. The MD simulations were run for 20 ± 3 ps with a time step of 1 fs. The results obtained by AIMD are in excellent quantitative agreement with the experimental results. All three interatomic potentials reproduce the thermal expansion well, with FS and ADP somewhat overestimating while MEAM slightly underestimating the DFT and experimental values.

B. Phonon dispersion

Vibrational properties are essential for analysis of finite-temperature behavior as well as migration of vacancies. We computed phonon dispersion spectra using all potentials by means of the small displacement method as implemented in the PHONOPY software package [87]. Figure 2 shows the phonon dispersions along high-symmetry directions, in comparison with the experimental data of Powell *et al.* [88] and DFT results. [54] We can see that all three potentials give similar results that are in accordance with the experimental data apart from small differences in frequencies at some zone boundaries. All potentials exhibit a softening of the LA 2/3[111] branch, but this weak softening related to the ω lattice instability is unlikely to enhance self-diffusion as in high-temperature stabilized bcc Ti or Zr [89,90].

Figure 2 also contains a comparison of phonon densities of states (DOS) for all potentials with DFT reference data [54]. All potentials provide a good qualitative description of the phonon DOS. The best quantitative agreement with the DFT reference data is obtained for the MEAM potential.

C. Vacancy properties at zero temperature

As mentioned above, zero temperature properties of point defects are often used during construction of interatomic potentials. We calculated the formation and migration energies for a monovacancy at zero pressure and zero temperature as

$$E^f_{\text{vac}} = E_{N-1} - \frac{N-1}{N} E_N, \tag{1}$$

TABLE II. Fundamental properties of a monovacancy in bcc Mo (energies are given in eV, entropies in units of k_B, attempt frequencies in THz).

	Exp.	DFT	FS	MEAM	ADP
$E^f_{\rm vac}$	3.0 ± 0.2[a]	2.80	2.55	2.96	2.81
	3.24 ± 0.09[b]	2.97[f]			
	3.2 ± 0.1[c]	3.10[g]			
		3.0, 2.9[i]			
		3.13, 2.90[j]			
$S^f_{\rm vac}$	1.5[c]	0.7[g]	2.32	0.51	1.96
	2.6 ± 0.4[b]				
$E^m_{\rm vac}$	1.23 ± 0.05[d]	1.20	1.30	1.65	1.30
	1.30 ± 0.02[e]	1.28[f]			
	1.62 ± 0.27[b]	1.29[h]			
	1.35 ± 0.05[c]	1.30[g]			
Γ_0		15[g]	89	64	44

[a]Reference [91].
[b]Reference [93].
[c]Reference [92].
[d]Reference [96].
[e]Reference [94].
[f]Reference [95].
[g]Reference [19].
[h]Reference [42].
[i]Reference [97].
[j]Reference [98].

where N is the number of atoms in the supercell without any defects (250- and 128-atom supercells were used for classical potentials and DFT, respectively), and E_N and E_{N-1} are the corresponding energies of a perfect bulk supercell and of a supercell containing a single vacancy where all atomic positions were relaxed, respectively.

According to Table II, MEAM and ADP predict a vacancy formation energy $E^f_{\rm vac}$ about 10% lower than the average experimental value, [91–93] while for the FS potential the energy is underestimated by about 20%. Note that the experimental energies [91–93] were obtained at high temperature and extrapolated to 0 K assuming temperature-independent formation quantities.

We also investigated the stability of divacancies. According to DFT calculations [99], the interaction between two vacancies in bcc Mo is weak; slightly attractive (positive binding energy) for the first-nearest-neighbor (1NN) configuration while repulsive (negative binding energy) for the second-nearest-neighbor (2NN) configuration. The FS and MEAM potentials predict the correct hierarchy of the energies with an overestimation of the attraction between vacancies. The ADP shows vacancy repulsion also for the 1NN configuration. The absolute binding energies, summarized in Table III, are small for all models and hence divacancies are not expected to occur frequently in the simulations and to contribute significantly to diffusion.

To calculate the vacancy migration energy $E^m_{\rm vac}$ at zero pressure and zero temperature, we employed the nudged elastic band (NEB) method [95,100]. Here we show only the nearest-neighbor vacancy jump along the ⟨111⟩ direction. The energy profiles along the minimum-energy path (MEP) are plotted in Fig. 3. We also investigated the second-nearest-neighbor jump along the ⟨100⟩ direction. The migration energies of 4.3, 3.9, and 4.0 eV obtained for the FS, MEAM, and ADP potentials, respectively, are significantly larger than those for the nearest-neighbor jumps.

TABLE III. Binding energies of 1NN and 2NN divacancies (in eV). The DFT data are taken from Ref. [99].

	DFT	FS	MEAM	ADP
1NN	0.05	0.30	0.20	−0.23
2NN	−0.22	−0.02	−0.04	−0.07

Results of our DFT calculations agree well with those of Nguyen-Manh *et al.* [95] who employed an atomiclike localized basis as implemented in the Plato code. Our DFT values of formation and migration energies are slightly lower than the values found in Ref. [95] which may be attributed to the different basis sets. Dense k-point sampling is necessary to obtain accurate and well converged migration energies and NEB profiles. For the 53-atom cell a k-point sampling smaller than 5×5×5 results in a double-hump NEB profile with a local minimum in the middle of the MEP. From the classical potentials, FS shows the best agreement with the DFT results, both in terms of barrier height and shape. The ADP potential predicts correctly the height of the migration barrier, but its shape is qualitatively different. We verified that the barrier is not affected by the size of the system (no significant changes exist for systems containing 53, 127, and 249 atoms) or the number of images (11, 21, and 41 were used). The largest discrepancy is obtained for the MEAM potential which overestimates the migration barrier by more than 0.3 eV. If we exclude the oldest experimental data [93], both FS and ADP potentials agree closely with experimentally estimated migration barriers.

The vacancy formation entropy $S^f_{\rm vac}$ corresponding to $T = 300$ K was obtained from the difference between the vi-

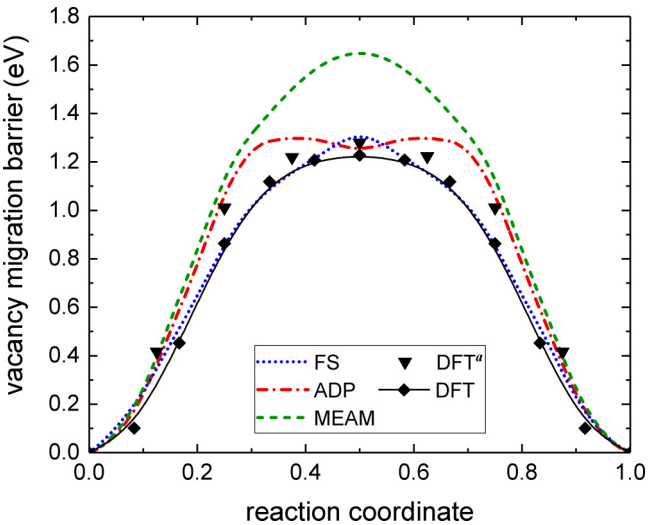

FIG. 3. A comparison of energy profiles along the minimum energy path for vacancy migration along the ⟨111⟩ direction in bcc Mo. Black triangles (DFT[a]) mark results from Ref. [95].

brational entropies of the bulk supercell and the supercell containing a vacancy, both relaxed to zero pressure. [101] The vibrational entropies were evaluated by integrating the phonon DOS [102,103] calculated using the software package PHONOPY.[87] We obtained similar values of $S^f_{\rm vac}$ for the FS ($2.32k_B$) and ADP ($1.96k_B$) potentials while a significantly smaller value of $0.51k_B$ was found for MEAM. The obtained results agree well with other vacancy formation entropies obtained for bcc metals (about $1-3k_B$) [4,50,104].

In addition, we employed transition state theory (TST) to estimate the attempt frequencies Γ_0 and vacancy jump rates Γ (see below) for all interatomic potentials. Specifically, we utilized two commonly used TST approaches derived by Eyring [105] and by Vineyard [106]. According to Eyring's TST, the jump rate can be expressed as

$$\Gamma = \frac{k_bT}{h}\exp\left(-\frac{\Delta F_{\rm vib}}{k_bT}\right)\exp\left(-\frac{E^m_{\rm vac}}{k_bT}\right) = \Gamma_0\exp\left(-\frac{E^m_{\rm vac}}{k_bT}\right), \quad (2)$$

where k_B and h are the Boltzmann and Planck's constants, and $\Delta F_{\rm vib}$ is the difference between vibrational free energies of the transition and equilibrium states. In Vineyard's approach, the attempt frequency is approximated as

$$\Gamma_0 = \frac{\prod_{n=1}^{N}\nu_n}{\prod_{m=1}^{N-1}\nu^*_m}, \quad (3)$$

where ν_i and ν^*_i are the Γ-point phonon frequencies for supercells corresponding to the equilibrium and transition states, respectively, and N is the number of modes (except for the translation modes). Both approaches become equivalent at high temperatures [107]. The phonon frequencies and vibrational free energies were evaluated using PHONOPY [87]. In order to ensure convergence, a dense q-mesh has been employed (up to $21\times21\times21$) to evaluate the free energies. The computed attempt frequencies from both approaches are almost identical and are listed in Table II.

III. PROPERTIES OF VACANCIES AT FINITE TEMPERATURES

Properties of monovacancies at absolute zero can be used to estimate diffusion as a function of temperature assuming Arrhenius relation. However, as mentioned in the Introduction, the energies and entropies of formation and migration may be temperature dependent.

Previous studies with classical potentials [10,21,22,49,50,108] and first-principles methods [13,14,19] have revealed that the vacancy formation energy may be strongly affected by anharmonicity, which leads to a marked nonlinear temperature dependence of vacancy concentration. However, much less is known about temperature dependence of the migration energy. In the following sections, we investigate the temperature variations of both formation and migration thermodynamic quantities in detail using various methodologies.

A. Temperature dependence of vacancy formation energy

The Gibbs free energy of vacancy formation $G^f_{\rm vac}$ determines the equilibrium vacancy concentration $c_{\rm vac}$ [10,13,49,109]. The equilibrium concentration at given temperature and pressure is described as

$$c_{\rm vac}(T) = \exp\left(-\frac{G^f_{\rm vac}(T)}{k_BT}\right) = \exp\left(\frac{S^f_{\rm vac}(T)}{k_B}\right)\exp\left(-\frac{H^f_{\rm vac}(T)}{k_BT}\right), \quad (4)$$

where $H^f_{\rm vac}$ and $S^f_{\rm vac}$ are the vacancy formation enthalpy and entropy, respectively. Since at zero pressure $H^f_{\rm vac} = E^f_{\rm vac}$, we will further use the term vacancy formation energy rather than enthalpy, unless the two quantities need to be distinguished. The focus of this section is to examine how the different interatomic potentials predict the temperature dependencies of $E^f_{\rm vac}$ and $S^f_{\rm vac}$ originating predominantly from anharmonicity of lattice vibrations [14,22].

1. Dependence of vacancy formation energy on the lattice expansion

As a first step, we considered how the vacancy formation energy varies with the expansion of crystal lattice, in absence of vibrational contributions. This calculation can be carried out with classical potentials as well as first-principles methods and hence serves as an additional benchmark of the employed models.

For this purpose, we used a supercell (127-atom for DFT, 249-atom for potentials) containing a single vacancy and gradually increased its volume up to the volume at the melting temperature. The vacancy formation energies were determined using Eq. (1) with respect to the bulk system at the same volume. The resulting dependencies of $E^f_{\rm vac}$ on lattice expansion, plotted as function of the effective temperature $T_{\rm eff}$ corresponding to the given expansion $\Delta a/a_0$ (cf. Fig. 1), are shown in Fig. 4. It is clearly seen that DFT as well as all three potentials predict an increase of $E^f_{\rm vac}$ with $T_{\rm eff}$ (i.e., with increasing volume). This increase is almost linear for DFT, MEAM, and ADP while FS gives a much weaker, nonlinear dependence.

The quasistatic dependence of $E^f_{\rm vac}$ on volume, which can be related to an effective temperature, suggests that the vacancy formation energy is likely to increase with increasing temperature. However, a rigorous determination of the vacancy formation energy at finite temperature requires an explicit consideration of atomic vibrations as obtained in MD simulations.

2. Vacancy formation energy from MD simulations

We performed extensive finite-temperature MD simulations using the NVT and NPT ensembles and large simulation cells containing $N = 432$ atoms for the bulk system and 431 atoms for the system with a single vacancy. As the formation energies are obtained by subtracting ensemble averages of highly fluctuating potential energies E_N and E_{N-1}, the MD simulations need to follow the system for extended time at each T [13,110]. Reliable sampling can be therefore

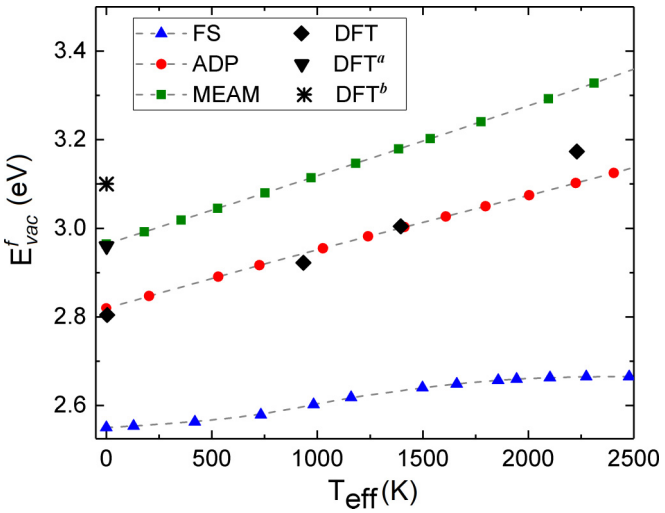

FIG. 4. Dependence of monovacancy formation energy on the effective temperature T_{eff}. Additional DFT results marked by superscripts ^{a} and ^{b} were taken from Refs. [95] and [19], respectively.

performed only with classical potentials. All MD simulations in our study were carried out for 30 ns, but even such long times do not completely remove scatter in obtained E^f_{vac} values since the instantaneous variations of the total energy of the system (especially at high temperatures) exceed significantly the absolute value of the vacancy formation energy (see the Appendix). Because of this sensitivity, it is necessary to examine all aspects that may affect the results.

The NVT simulations were carried out at the volume corresponding to perfect bulk system at zero pressure for each temperature considered. As the volume for vacancy-containing supercells should be slightly smaller, unrelaxed systems with a vacancy are under small tensile hydrostatic stress. In NPT simulations, the pressure was set to zero which led to small differences in the volumes obtained for systems with and without vacancy. The thermostat dumping parameter regulating P and T was set to 10 ps. We did not impose any restrictions on atoms during the MD simulations, so that the vacancy can migrate and the average potential energy of the system takes into account various possible defect positions.

The temperature dependencies of E^f_{vac} evaluated for all three interatomic potentials are plotted in Fig. 5. The results of both NVT and NPT simulations (marked by empty and full symbols, respectively) consistently show a nonlinear increase of E^f_{vac} with temperature for all potentials. The NVT results exhibit a scatter of about ± 0.25 eV while the thermostatting/barostatting in NPT simulations leads to a better convergence and reduces the error in determining $E^f_{\text{vac}}(T)$ at a given temperature to ± 0.15 eV. For MEAM and ADP, the NVT simulations overestimate E^f_{vac} values for $T > 1000$ K in comparison with the NPT results. Figure 5 includes also DFT results from Ref. [19] that show a similar trend but are shifted due to likely overestimation of the vacancy formation energy by the AM05 exchange-correlation functional.

The NPT results were fitted using second- and fourth-order polynomials (thin and thick dotted lines in Fig. 5). For the FS potential, the second-order polynomial captures the temperature dependence of E^f_{vac} very closely while for the ADP and MEAM potentials fourth-order polynomials are necessary to describe the sharp increases of E^f_{vac} at high temperature. By using the thermodynamic relation $T\,dS/dT = dH/dT = dE/dT$ and the calculated entropy at room temperature (see Table II), we obtained the temperature dependence of the vacancy formation entropy S^f_{vac}, also shown for all three potentials in Fig. 5 (bottom right). Although they yield qualitatively different trends, the vacancy formation entropy increases monotonously with T for all three potentials. It is obvious that for $E^f_{\text{vac}} \sim T^2$ the entropy is a linear function of temperature (as for the FS potential) while nonlinear $S^f_{\text{vac}}(T)$ dependencies are obtained for the ADP and MEAM potentials. The differences among the predictions of MEAM, ADP, and FS models are reminiscent of those reported recently for fcc aluminum. For temperatures ranging from 300 K to the Al melting point, *ab initio* and neural-network potential (trained on DFT data) calculations indicated linear versus nonlinear dependences of S_f on T, respectively [13,111]. Hence, these results as well as our findings suggest that a monotonous increase of S_f with T may be common to various metals and possibly cause deviations from Arrhenius trends in self-diffusivities. Furthermore, the assumption of a linear temperature dependence of the vacancy formation entropy, which was used in various studies [13,19,23], may not be generally valid.

In comparison with the linear increase of E^f_{vac} with the effective temperature (cf. Fig. 4), the obtained results clearly indicate that the explicit inclusion of vibrational contributions leads to much stronger and nonlinear temperature dependencies of E^f_{vac} due to anharmonic effects.

From the knowledge of $E^f_{\text{vac}}(T)$ we can compute the Gibbs free energy G of vacancy formation by integrating the Gibbs-Helmholtz equation,

$$\frac{G^f_{\text{vac}}(T)}{T} = \frac{E^f_0 - T_0 S^f_0}{T_0} - \int_{T_0}^{T} \frac{E^f_{\text{vac}}(T')}{T'^2} dT',$$

$$G^f_{\text{vac}}(T) = E^f_0 \frac{T}{T_0} - T S^f_0 - T \int_{T_0}^{T} \frac{E^f_{\text{vac}}(T')}{T'^2} dT', \qquad (5)$$

where T_0 is a reference temperature (taken as 300 K), and E^f_0 and S^f_0 are the vacancy formation energy and entropy, respectively, at T_0 and zero pressure.

The predicted temperature variations $G^f_{\text{vac}}(T)$ are also displayed in Fig. 5, for both second- and fourth-order polynomial fits. In addition, we also included linear dependencies $G^f_{\text{vac}} = E^f_0 - T S^f_0$ (dot-dashed lines) for comparison and in order to highlight the deviations from the Arrhenius behavior due to anharmonic effects. The results in Fig. 5 clearly show that the standard evaluation of vacancy free energies based on constant formation enthalpies and entropies is applicable only at low temperatures. For elevated temperatures all three potentials predict strong deviations from the linear behavior.

Figure 6 summarizes the predicted temperature dependencies of the vacancy concentration. Assuming temperature

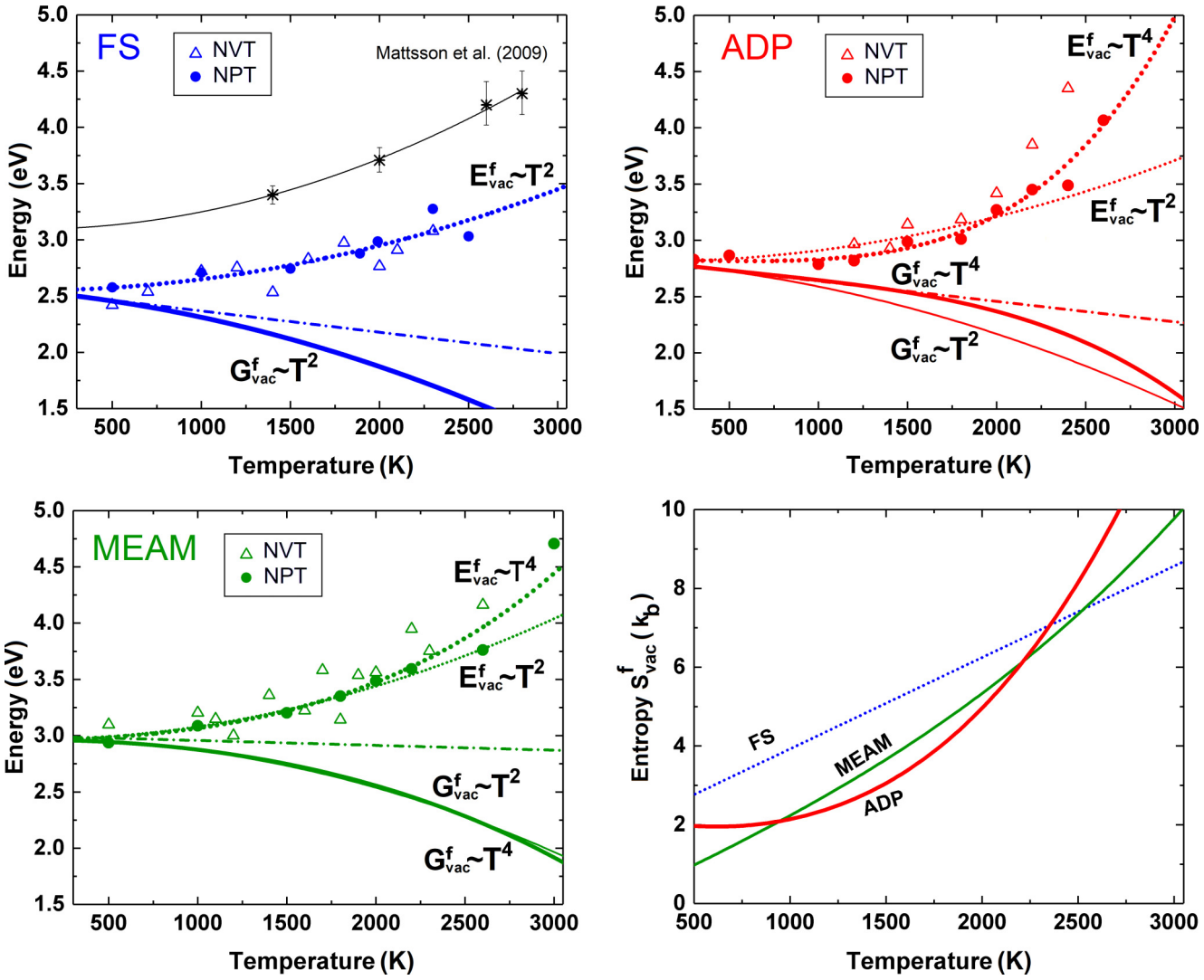

FIG. 5. Temperature dependencies of the vacancy formation energies: dotted lines—$E^f_{\rm vac}(T)$; solid lines—$G^f_{\rm vac}(T)$; dot-dash lines—$G^f_{\rm vac}$ based on temperature-independent $E^f_{\rm vac}$. The MD results for NVT and NPT simulations are marked by symbols. DFT results from Ref. [19] are shown in the FS graph. The temperature dependence of the vacancy formation entropy $S^f_{\rm vac}$ is plotted in the bottom right panel.

independent vacancy formation enthalpies and entropies (cf. Table II), we obtain a linear Arrhenius behavior for all three potentials, marked by straight dashed lines in Fig. 6. When taking into account the nonlinear temperature dependencies of the free energies originating from anharmonic effects (cf. Fig. 5), the predicted vacancy concentrations are strongly enhanced at elevated temperatures and deviate from the Arrhenius behavior for all potentials (marked by full lines in Fig. 6). The figure contains also results extracted from large-scale MD simulations discussed in Sec. IV.

The extrapolated vacancy concentrations at the corresponding melting temperatures of the three potentials are 0.04%, 0.2%, and 0.4% for ADP, MEAM, and FS, respectively. These theoretically predicted vacancy concentrations are about one to two orders of magnitude larger than experimental estimations from resistivity measurements [92,93], marked by black lines in Fig. 6. Possible origins of this discrepancy will be discussed below.

The concentration of divacancies $c_{\rm 2vac}$ depends on the concentration of single vacancies and their binding energy as $c_{\rm 2vac} \approx c^2_{\rm vac} \exp(E_b/kT)$. Thus, even at the melting temperature $c_{\rm 2vac}$ is about 3–4 orders lower than $c_{\rm vac}$ and the contribution of divacancies to self-diffusion can be neglected.

B. Temperature dependence of vacancy migration energy

In this section, we use several complementary methods to evaluate the vacancy migration at finite temperatures. This allows us to assess the accuracy of each method as well as the consistency of the results.

1. Dependence of vacancy migration energy on the lattice expansion

We first evaluated the dependence of the vacancy migration energy on volume and related it to an effective temperature based on the thermal expansion of the lattice. The calculations

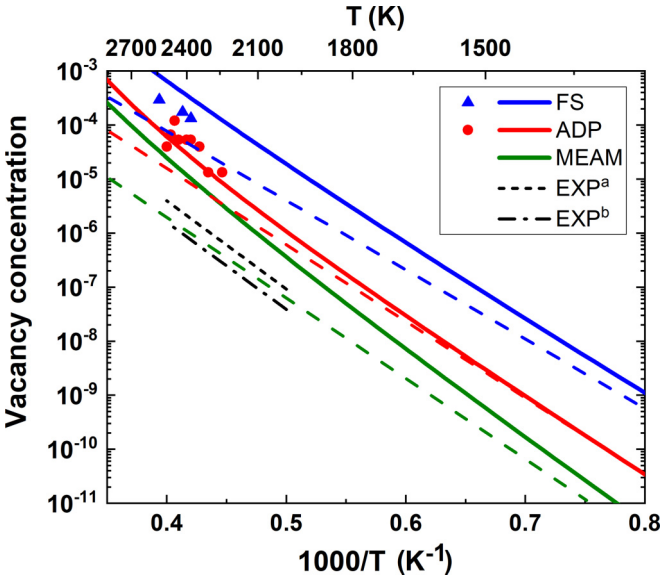

FIG. 6. A comparison of experimental and theoretical vacancy concentrations as function of temperature; dashed lines correspond to Arrhenius dependencies based on formation energy/entropy at zero temperature, full lines take into account the temperature dependence of $E^f_{\rm vac}$ and $S^f_{\rm vac}$, points correspond to results of direct MD simulations (see Sec. IV). The experimental data were taken from Refs. [93] (^{a}) and [92] (^{b}).

were performed using classical potentials as well as DFT. The results are plotted in Fig. 7. The DFT migration barrier remains almost constant as the volume increases. In contrast, all classical potentials predict a similar linear increase of the migration barrier with increasing $T_{\rm eff}$ (i.e., with increasing volume).

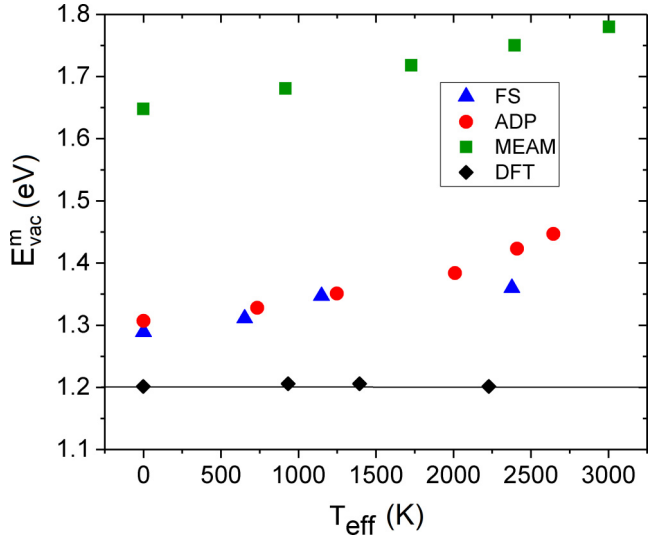

FIG. 7. Dependence of vacancy migration energy on the effective temperature $T_{\rm eff}$.

2. Evaluation of the migration free energy via transition interface sampling

Transition interface sampling (TIS) [55,112] is a method for computing kinetic properties of diffusive processes associated with crossing of a large free energy barrier, i.e., rare events on the time scale accessible to molecular dynamics. The TIS method employs a Monte Carlo (MC) framework in trajectory space to sample the ensemble of phase space trajectories between two stable states A and B (the initial and final position of the vacancy) separated by a free energy barrier. This allows for a direct evaluation of the migration rate. In the TIS framework a set of nonintersecting interfaces defined by a progress order parameter λ_i are introduced between the stable states. We sampled the ensemble of trajectories using a shooting algorithm [113], where a slight perturbation of the momenta is performed for a configuration randomly selected from a trial migration path. A new trajectory is then generated by integrating the equations of motion forward and backward in time from the modified configuration. This trajectory is accepted in the MC step if it crosses the interface λ_i and starts and ends in one of the stable states A or B. The migration rate Γ, i.e., the number of vacancy jumps per unit time, is then calculated from the product of the flux through the first interface $\langle\phi\rangle_0$ and the probability $P(\lambda_B|\lambda_A)$ that a trajectory reaches state B given that the system has crossed the first interface,

$$\Gamma = \langle\phi\rangle_0 P(\lambda_B|\lambda_A), \tag{6}$$

where the flux $\langle\phi\rangle_0$ is calculated using MD simulations in the initial state A and counting the number of positive crossings per unit time [55,114]. The crossing probability from A to B is calculated by matching the individual crossing histograms obtained from the path ensemble per interface $P(\lambda_{i+1}|\lambda_i)$ with the weighted histogram analysis method [115].

The TIS simulations were performed using a python wrapper together with the LAMMPS code. The MD trajectories were created in the NVT ensemble with a Nosé-Hoover thermostat and a time step of 0.5 fs for all simulations. A $4 \times 4 \times 4$ supercell containing 127 atoms with a single vacancy and minimum image periodic boundary conditions was used in all simulations. The path ensembles were sampled using the replica exchange TIS approach [116,117]. For each temperature, we performed at least 1500 moves per interface with a combination of 45% shooting moves, 45% of exchange moves and 10% exchanges between forward (AB) and backward (BA) ensembles. The order parameter used in the TIS simulations is the distance $\lambda = d_{\rm vac}$ between the equilibrium position of the vacancy and a selected atom chosen from its first nearest neighbors. The definitions of the stable-state regions (first interface) and all the interfaces are listed in the Appendix. The positions of interfaces were selected such that there was at least 10% overlapping of the corresponding crossing histograms. The diffusivities obtained from the TIS simulations are shown in Fig. 9.

3. Evaluation of the migration free energy via thermodynamic integration

Alternatively, the migration free energy may be obtained using a thermodynamic integration (TI). This approach is

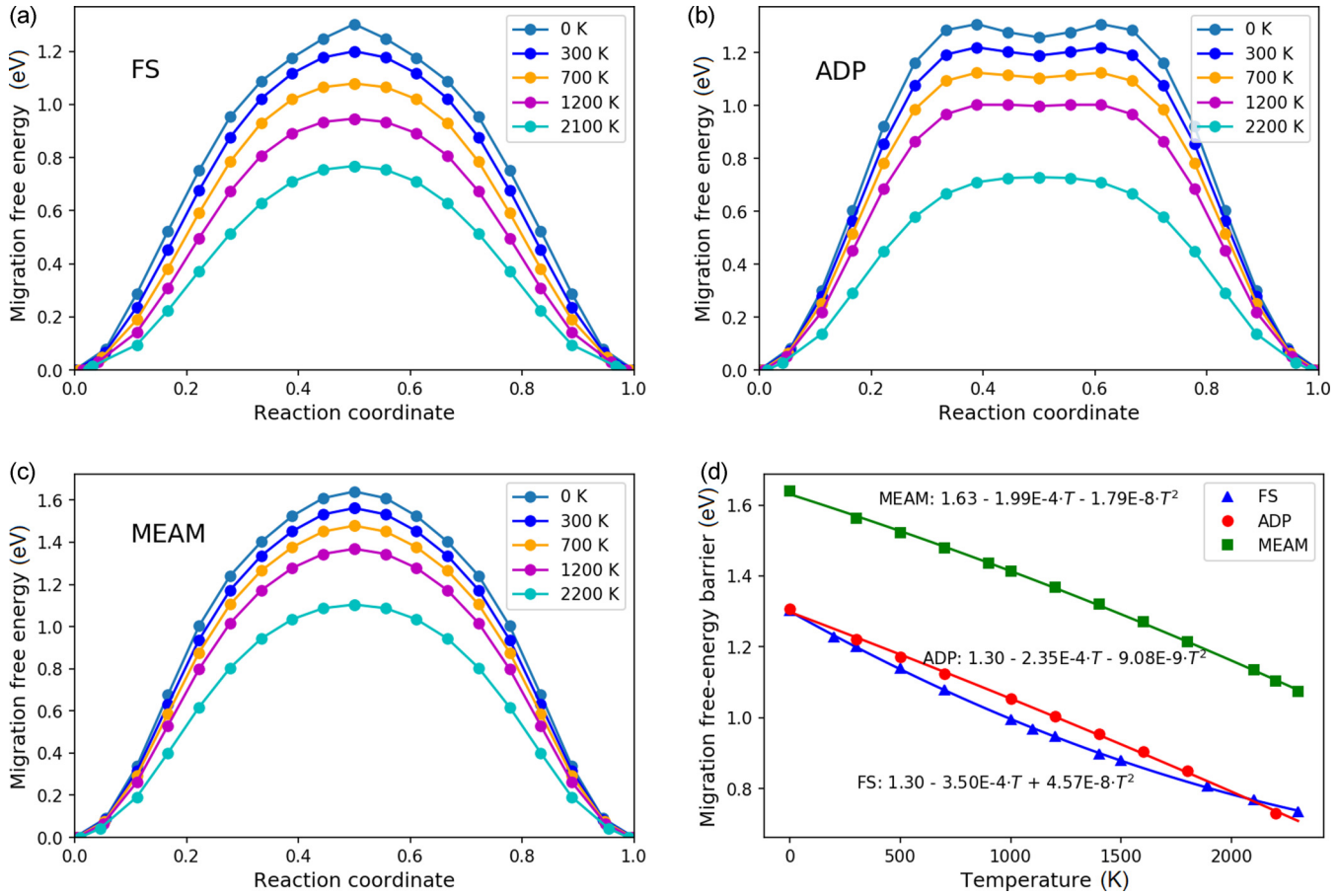

FIG. 8. The migration free-energy profiles for FS (a), ADP (b), and MEAM (c) at different temperatures. (d) The temperature-dependent migration free-energy barriers (dots) and second-order polynomial fits (solid lines).

based on the observation that the derivative of the migration free energy $G^m_{\rm vac}(T)$ with respect to the migration distance μ_m is equal to the negative of the mean force on the migrating atom projected along the migration path,

$$\frac{\partial G^m_{\rm vac}(T)}{\partial \mu_m} = -\langle \mathbf{F}_m \cdot \mathbf{e}_m \rangle_{\mu_m}, \tag{7}$$

where $\mathbf{F}_m$ is the atomic force on the migrating atom and $\mathbf{e}_m$ is the migration direction. The subscript μ_m on the right-hand side denotes that the thermal average is taken at a given migration distance. We evaluated Eq. (7) in the NVT ensemble with thermal expansion taken into account via the temperature-dependent lattice parameter (cf. Fig. 1). The migration free-energy profile is then obtained by integrating Eq. (7) along the migration path.

Our results are shown in Fig. 8. The free-energy barriers decrease with increasing temperature for all three interatomic potentials, which indicates that the vibrational entropy for the saddle point configuration is larger than that of the vacancy in equilibrium. A second-order polynomial fit of the migration free-energy barrier gives very small second-order coefficients for all three interatomic potentials. As the non-Arrhenius behavior gives rise to the second-order terms, these results indicate that the anharmonic contributions to the migration free energy are small.

4. Atomistic simulation of single-vacancy diffusion

The most direct way to obtain $D_{\rm vac}$ is via MD simulations of single vacancy diffusion. We performed a series of MD simulations using periodic supercells containing 1999 Mo atoms (i.e., 2000 atoms arranged in a bcc lattice with a single vacancy). Each simulation was carried out in the NVE ensemble, with the volume adjusted to obtain zero pressure. The diffusion coefficients were extracted from the mean-square displacements (δr_i^2) of all atoms in the system as

$$D_{\rm vac} = \sum_{i=1}^{N} \delta r_i^2 / 6t. \tag{8}$$

MD times of 2 ns were found sufficient for reliable determination of $D_{\rm vac}$ at high temperatures while much longer times of up to 50 ns were necessary to achieve a sufficient number of jump events at lower temperatures. The obtained diffusivities were used for evaluation of the self-diffusion coefficients (see the final section).

5. Summary of single-vacancy diffusion results

A summary of single-vacancy diffusivities evaluated using TIS (empty symbols), TI (full lines), and MD (full symbols) methods, together with Arrhenius relations obtained from TST (dashed lines) based on attempt frequencies and migra-

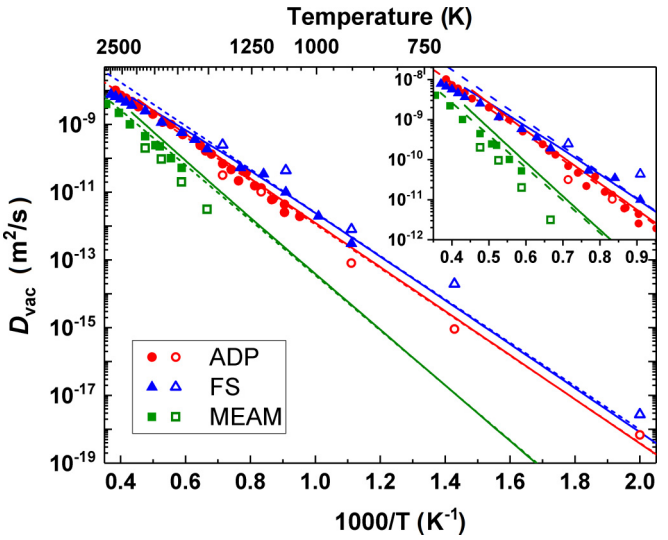

FIG. 9. Single-vacancy diffusivities calculated with three different interatomic potentials. Dashed lines correspond to temperature independent TST rates (i.e., Arrhenius behavior), solid lines mark TI results, the open and solid symbols correspond to TIS and MD results, respectively.

tion barriers at $T = 0$ (cf. Table 2) is presented in Fig. 9 for the temperature range of 500–2850 K.

For each interatomic potential, all methods provide consistent results with some quantitative differences. Overall, the observed deviation from the linear Arrhenius behavior is small and significant only for the FS potential at high temperature (see the inset in Fig. 9). As expected, the slopes are consistent at low temperatures with the calculated zero-temperature migration barriers. Near the melting temperature all considered models converge to similar values of about 10^{-8} m^2/s.

IV. DIRECT MD SIMULATIONS OF SELF-DIFFUSION

The calculations presented in the previous Section examined the temperature dependence of vacancy formation and migration separately. The computational efficiency of classical interatomic potentials enables one to follow the complete process of self-diffusion, including the spontaneous creation and migration of defects directly in large-scale molecular dynamics simulations. Even though sufficient statistical sampling and equilibrium conditions can still be reached only for elevated temperatures, such simulations provide independent insights and additional validation. We conducted a series of MD simulations using the ADP and FS potentials. High computational costs did not allow us to obtain converged results for the MEAM potential.

The MD simulation blocks consisted of a slab with two free surfaces that mimic a system with open boundaries. This simulation setup was employed previously in a study of equilibrium defect concentration in iron [50]. The main purpose of the free surfaces is to regulate the formation and removal of point defects that govern diffusion in the system. The defects are generated spontaneously due to thermal fluctuations, either at the surface or in the bulk as Frenkel pairs. This simulation setup therefore imposes no restrictions

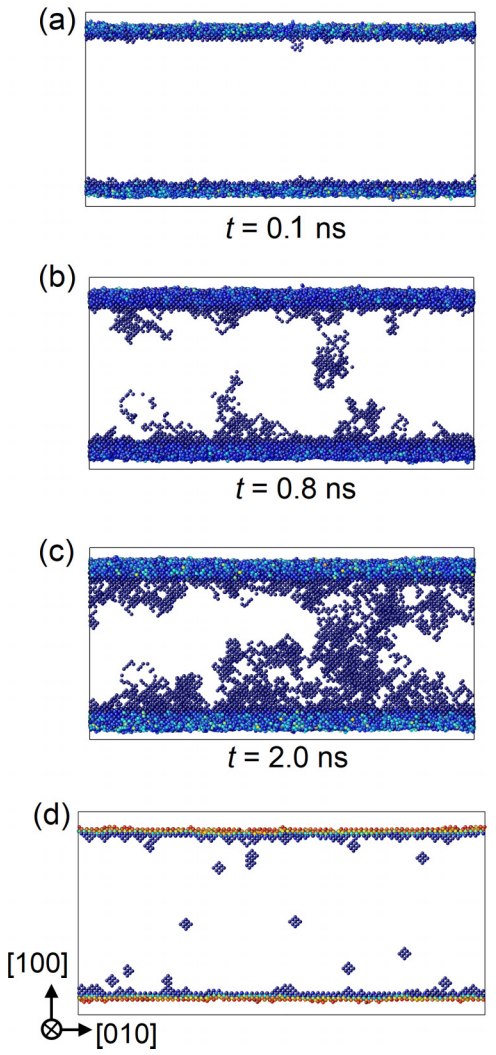

FIG. 10. Snapshots from MD simulations at $T = 2400$ K with open surfaces. Panels (a)–(c) show evolution of defects and their trajectories during the MD run (only atoms with the highest displacements are drawn); panel (d) depicts the final configuration quenched to $T = 0$ where only atoms with the highest potential energy, i.e., surface atoms and atoms surrounding vacancies are shown.

on the type of defect that may be present, in contrast to bulk systems without free surfaces where the formation of Frenkel pairs is the only possible way how point defects can be generated. As the Frenkel pair has a very high formation energy (>8 eV in bcc Mo), its formation is rare. Provided that the open system is simulated for a sufficiently long time, it is possible to estimate not only the types (i.e., monovacancy, divacancy, interstitial, etc.) and concentrations of the point defects at given conditions but also the overall self-diffusion coefficient D_{self}. Our previous simulations for Zr [16] revealed that point defect concentration reaches its equilibrium value after $t \approx 0.5$ ns at $T \approx 0.7T_m$.

Figure 10 presents several snapshots illustrating the evolution of the system simulated for T ≈ 2400 K using the ADP potential (only atoms with large displacements are shown). The size of our models was $40a \times 80a \times 30a$ (a is the lattice parameter) along the $x = [100]$, $y = [010]$ and

$z = [001]$ crystallographic directions. The free surfaces were oriented perpendicular to the x direction and had a total area of $2 \times 2400a^2$ Å^2, which was sufficient for a spontaneous and independent creation and annihilation of defects.

The total number of atoms in the the block was 165 600. For a reliable evaluation of the diffusion coefficients, we divided the block into three regions—two regions within $10a$ from each surface (containing in total 91 200 atoms), and a central region in between (containing in total 74 400 atoms) for which the diffusion coefficient was evaluated from the mean-square displacements (MSD) of atoms (δr_i^2) as $D_{\text{self}} = N^{-1} \sum_{i=1}^{N} \delta r_i^2/6t$, where N is the number of atoms in the central region and t is the simulation time. The exclusion of the surface regions ensures that the predicted self-diffusivities indeed correspond to bulk values and are not affected by any surface effects. Our tests show that the thickness of the surface region can be decreased to $5a$ without affecting the obtained diffusion coefficients significantly.

All MD simulations were performed in the NVE ensemble at lattice parameters corresponding to the simulated temperatures. It should be noted that the temperature slightly decreases during equilibration due to formation of defects, but this decrease is negligible (about 2–3 K during the first nanosecond). Typical simulation times were about 2.5 ns after equilibration. Equilibrium defect concentrations could only be reached for simulation temperatures close to the melting point.

By tracking the number of defects present in the bulk region during the simulation we were able to determine whether the equilibrium concentration has been reached. This was done by quenching the atomic configurations to zero temperature at regular intervals during the MD run and detecting atoms with high potential energies. Such approach yields both the number of defects in the system and their positions. An additional validation of the steady state conditions is obtained from the evaluation of D_{self} via MSD(T) when the slope does not change once the equilibrium has been reached [16].

The large-scale MD simulations reveal that for both interatomic potentials and all temperatures investigated the only type of defect present is the monovacancy. This outcome is consistent with experimental observations [91] as well as theoretical assumptions as the formation energies of divacancies and self-interstitials in bcc Mo are significantly (about 2–3 times) larger than that of a monovacancy [118–121]. We also did not observe any diffusion via concerted motion of several atoms, as found recently for Ti. [90]

The vacancy concentrations extracted from the MD simulations are included in Fig. 6 (FS and ADP results are marked by triangles and circles, respectively). They agree well with the non-Arrhenius dependence obtained from the temperature dependent formation free energies, and further confirm the deviations due to anharmonicity at high temperatures.

V. DISCUSSION AND CONCLUSIONS

The final outcome of our study summarizing both theoretical and experimental self-diffusion coefficients in bcc Mo is presented in Fig. 11. The most recent experimental data from Ref. [32] that cover a broad temperature range are marked by black squares together with additional high-temperature

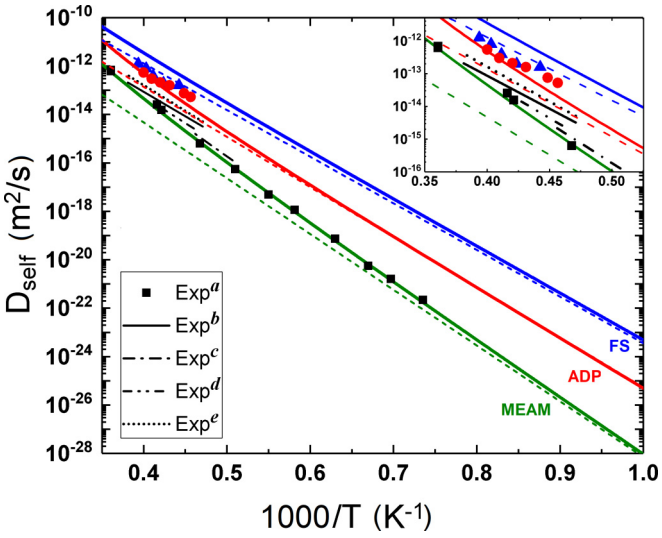

FIG. 11. A comparison of theoretical and experimental temperature dependencies of self-diffusion coefficients for bcc Mo; blue triangles and red circles show the results of the direct large-scale MD simulations performed with FS and ADP potentials, respectively; bold solid and thin dashed lines correspond to $c_{\text{vac}}D_{\text{vac}}$ with temperature-dependent and temperature-independent energies, respectively. The experimental data (Refs. [32,122–125]) are marked by superscripts.

experimental results plotted by black lines [122–125]. The analytic predictions of $D_{\text{self}} = c_{\text{vac}}D_{\text{vac}}$ are shown in Fig. 11 by lines, with dashed and full lines corresponding to temperature independent, i.e., Arrhenius-like, and temperature dependent vacancy free energies, respectively. For the latter case, it is evident that all three potentials predict a clear upward curvature of D_{self}, which is most pronounced for the MEAM potential. The self-diffusion coefficients obtained directly from MD large-scale simulations using the FS and ADP potentials agree well with the analytic results.

The results compiled in Fig. 11 reveal that, among all considered vacancy characteristics, it is the temperature dependence of the vacancy formation energy that governs the non-Arrhenius behavior of D_{self} in bcc Mo. Even though single-vacancy diffusivities exhibit also deviations from Arrhenius behavior at elevated temperatures (see Fig. 9), these variations are insignificant in comparison with the changes of E_{vac}^f.

What remains puzzling is the discrepancy between the theoretically predicted vacancy concentrations (cf. Fig. 6) and experimental data. Our results as well as previous DFT estimates [19,42] consistently show vacancy concentrations close to the melting temperature that are one to two orders of magnitude larger than those obtained from resistivity measurements [92,93]. Even though these measurements tend to be very accurate, there are several sources of uncertainties when interpreting the experimental data, namely, the amount of impurities, vacancy loss during quenching, and the value of specific resistivity associated with a single vacancy, which is needed to convert the measured resistivity values to absolute vacancy concentrations. It is obvious from the existing resistivity analyses [92,93] as well as from other

techniques, such as positron annihilation spectroscopy or specific heat measurements [126], that the experimentally determined equilibrium vacancy concentrations close to the melting point are uncertain, spanning the range between 10^{-5} and 10^{-2}. It should also be noted that the experimental estimates typically assume a temperature-independent formation energy.

The present simulation results consistently show that there is a contribution from the anharmonicity of lattice vibrations that significantly increases the vacancy concentration at elevated temperatures. In this view, the interpretation of resistivity measurements therefore likely underestimates the quenching loss and/or overestimates the specific resistivity, resulting in vacancy concentrations that might be too low. However, it should be noted that the uncertainties of 0.2–0.3 eV in the computed 0 K formation energies and of more than 1 k_B in the formation entropies (cf. Table II) lead to variations in the predicted vacancy concentrations of more than one order of magnitude at elevated temperature and several orders of magnitude at low temperatures (see Fig. 6).

Finally, our in-depth validation of three widely used interatomic potentials for Mo provides valuable insights. The final comparison of self-diffusion coefficients in Fig. 11 shows a remarkable agreement between experimental data of Maier *et al.* [32] and theoretical predictions obtained by the MEAM potential. However, based on our analysis this result is fortuitous. As the MEAM potential strongly overestimates the vacancy migration energy in comparison to DFT, it exhibits a much steeper temperature dependence. Even more importantly, the melting temperature predicted by MEAM is more than 300 K higher than that of the other two potentials and the experimental value (cf. Table I), which leads to effectively lower c_{vac} at a given temperature. If the MEAM results were normalized to the melting temperatures of the other potentials, the MEAM and ADP self-diffusion coefficients would reach similar values of about 10^{-11} m^2/s at the melting point. The interatomic potentials therefore give similar descriptions of the temperature dependence of self-diffusion coefficient on the homologous temperature T/T_m, and the quantitative differences visible in Fig. 11 originate primarily from different values of the vacancy formation energies and entropies at $T = 0\,\mathrm{K}$.

In summary, our analysis employing static and dynamic atomistic calculations as well as statistical sampling techniques and thermodynamic integration shows that the peculiar non-Arrhenius self-diffusion behavior of bcc Mo is likely mainly caused by strong temperature dependence of the vacancy formation energy. This outcome, supported by other related theoretical studies, is of great importance for interpretation of future as well as past diffusion measurements. However, as the theoretically predicted temperature variations also exhibit significant scatter, a fully quantitative agreement between experiment and theory is still to be reached. The second main outcome of our study is related to in-depth validation of interatomic potentials. It is evident that the reliability of their predictions for complex materials phenomena such as self-diffusion cannot be ascertained based on a few fundamental properties but require a thorough multilevel assessment.

ACKNOWLEDGMENTS

M.N.P., D.S., and M.M. gratefully acknowledge the financial support under the scope of the COMET program within the K2 Center "Integrated Computational Material, Process and Product Engineering (IC-MPPE)" (Project No. 859480). This program is supported by the Austrian Federal Ministries for Transport, Innovation, and Technology (BMVIT) and for Digital and Economic Affairs (BMDW), represented by the Austrian research funding association (FFG), and the federal states of Styria, Upper Austria and Tyrol. Financial support from the Swedish Government Strategic Research Area in Materials Science on Functional Materials at Linköping University (Faculty Grant SFOMat-LiU No. 2009-00971), and the VINN Excellence Center Functional Nanoscale Materials (FunMat-2) Grant No. 2016–05156 is gratefully acknowledged by I.A.A. and D.G.S. G.D.L. acknowledges the financial support by the German Research Foundation (DFG) through Project No. RO 3073/6-1 and by the Mexican National Council for Science and Technology (CONACYT) through Project No. 232090. D.G.S. gratefully acknowledges financial support from the Olle Engkvist Foundation and supercomputer resources provided by the Swedish National Infrastructure for Computing (SNIC).

APPENDIX: SUPPLEMENTAL MATERIAL

Here we provide additional information regarding the simulations carried out in this work. Figure 12 shows potential energy variations obtained in MD simulations at different time-averaging. In Table IV we summarize data used for TIS simulations. Namely, Table IV contains definitions of the stable-state regions (first interface) and all the interfaces.

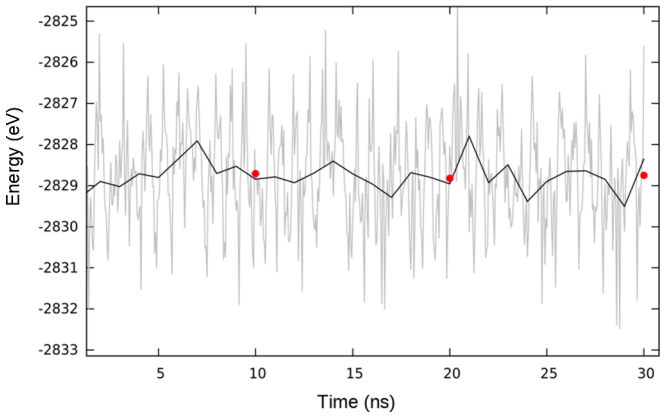

FIG. 12. An example of potential energy variations from an NVT MD simulation (using the FS potential) of 432 atom supercell containing a single vacancy at $T = 1600$ K; the gray lines, black lines, and red points correspond to averaging over 0.05, 1, and 10 ns, respectively.

TABLE IV. Positions of the interfaces at different temperatures for FS, ADP, and MEAM interatomic potentials.

T (K)	Interface positions d_{vac}
FS	
500	0.24, 0.36, 0.44, 0.48, 0.56, 0.6, 0.67, 0.72, 0.82, 0.90, 0.97, 1.09, 1.21, 1.37, 1.54, 1.64, 1.84, 1.91, 1.99, 2.06
700	0.32, 0.56, 0.6, 0.72, 0.76, 0.82, 0.89, 0.98, 1.02, 1.09, 1.23, 1.36, 1.64, 1.82, 1.91, 1.99, 2.06
900	0.37, 0.45, 0.52, 0.6, 0.63, 0.67, 0.72, 0.78, 0.82, 0.89, 1.09, 1.29, 1.37, 1.45, 1.64, 1.82, 1.91, 1.99, 2.06
1100	0.42, 0.52, 0.6, 0.67, 0.72, 0.82, 0.90, 1.09, 1.29, 1.37, 1.45, 1.64, 1.85, 1.91, 1.99, 2.06
1400	0.43, 0.6, 0.82, 0.97, 1.09, 1.37, 1.64, 1.91, 1.99, 2.06
1900	0.51, 0.6, 0.67, 0.72, 0.82, 0.88, 1.09, 1.18, 1.37, 1.45, 1.19, 1.37, 1.45, 1.64, 1.84, 1.91, 1.99, 2.06
ADP	
500	0.19, 0.24, 0.36, 0.44, 0.48, 0.56, 0.60, 0.67, 0.72, 0.82, 0.90, 0.97, 1.09, 1.21, 1.37, 1.54, 1.64, 1.84, 1.91, 1.99, 2.06
700	0.22, 0.25, 0.32, 0.38, 0.44, 0.56, 0.6, 0.72, 0.76, 0.82, 0.89, 0.98, 1.02, 1.09, 1.23, 1.37, 1.64, 1.82, 1.91, 1.99, 2.06
900	0.28, 0.32, 0.37, 0.44, 0.52, 0.6, 0.67, 0.78, 0.89, 0.97, 1.09, 1.29, 1.37, 1.45, 1.64, 1.82, 1.91, 1.99, 2.06
1200	0.34, 0.38, 0.42, 0.52, 0.6, 0.67, 0.72, 0.82, 0.90, 1.09, 1.29, 1.37, 1.45, 1.64, 1.85, 1.91, 1.99, 2.06
1400	0.32, 0.43, 0.6, 0.82, 0.97, 1.09, 1.37, 1.6, 1.64, 1.82, 1.9, 1.99, 2.06
1800	0.39, 0.47. 0.6, 0.82, 0.97, 1.09, 1.37, 1.57, 1.64, 1.82, 1.9, 1.99, 2.06
MEAM	
1500	0.34, 0.44, 0.56, 0.63, 0.72, 0.82, 0.92, 1.09, 1.18, 1.37, 1.64, 1.91, 1.99, 2.06
1700	0.38, 0.44, 0.56, 0.63, 0.72, 0.82, 0.92, 1.09, 1.18, 1.37, 1.64, 1.91, 1.99, 2.06
1900	0.4, 0.44, 0.56, 0.63, 0.72, 0.82, 0.92, 1.09, 1.18, 1.37, 1.64, 1.91, 1.99, 2.06
2100	0.45, 0.56, 0.63, 0.72, 0.82, 0.92, 1.09, 1.18, 1.37, 1.64, 1.91, 1.99, 2.06

[1] N. L. Peterson, J. Nucl. Mater. **69**, 3 (1978).
[2] A. Seeger, Defect Diffus. Forum **95**, 147 (1993).
[3] Y. Kraftmakher, Phys. Rep. **299**, 79 (1998).
[4] H. Mehrer, *Diffusion in Solids: Fundamentals, Methods, Materials, Diffusion-controlled Processes*, Vol. 155 (Springer Science & Business Media, Berlin, 2007).
[5] G. Neumann and C. Tuijn, *Self-diffusion and Impurity Diffusion in Pure Metals: Handbook of Experimental Data*, Vol. 14 (Elsevier, Amsterdam, 2011).
[6] C. Freysoldt, B. Grabowski, T. Hickel, J. Neugebauer, G. Kresse, A. Janotti, and C. G. Van de Walle, Rev. Mod. Phys. **86**, 253 (2014).
[7] J. Rogal, S. V. Divinski, M. W. Finnis, A. Glensk, J. Neugebauer, J. H. Perepezko, S. Schuwalow, M. H. F. Sluiter, and B. Sundman, Phys. Status Solidi B **251**, 97 (2014).
[8] S.-L. Shang, B.-C. Zhou, W. Y. Wang, A. J. Ross, X. L. Liu, Y.-J. Hu, H.-Z. Fang, Y. Wang, and Z.-K. Liu, Acta Mater. **109**, 128 (2016).
[9] K. Carling, G. Wahnström, T. R. Mattsson, A. E. Mattsson, N. Sandberg, and G. Grimvall, Phys. Rev. Lett. **85**, 3862 (2000).
[10] K. M. Carling, G. Wahnström, T. R. Mattsson, N. Sandberg, and G. Grimvall, Phys. Rev. B **67**, 054101 (2003).
[11] M. Mantina, Y. Wang, R. Arroyave, L. Q. Chen, Z. K. Liu, and C. Wolverton, Phys. Rev. Lett. **100**, 215901 (2008).
[12] M. Mantina, Y. Wang, L. Q. Chen, Z. K. Liu, and C. Wolverton, Acta Mater. **57**, 4102 (2009).
[13] A. Glensk, B. Grabowski, T. Hickel, and J. Neugebauer, Phys. Rev. X **4**, 011018 (2014).
[14] A. Glensk, B. Grabowski, T. Hickel, and J. Neugebauer, Phys. Rev. Lett. **114**, 195901 (2015).
[15] S. V. Starikov, L. N. Kolotova, A. Y. Kuksin, D. E. Smirnova, and V. I. Tseplyaev, J. Nucl. Mater. **499**, 451 (2018).
[16] D. E. Smirnova, S. V. Starikov, and I. S. Gordeev, Comput. Mater. Sci. **152**, 51 (2018).
[17] R. Nazarov, T. Hickel, and J. Neugebauer, Phys. Rev. B **85**, 144118 (2012).
[18] B. Medasani, M. Haranczyk, A. Canning, and M. Asta, Comput. Mater. Sci. **101**, 96 (2015).
[19] T. R. Mattsson, N. Sandberg, R. Armiento, and A. E. Mattsson, Phys. Rev. B **80**, 224104 (2009).
[20] T. Angsten, T. Mayeshiba, H. Wu, and D. Morgan, New J. Phys. **16**, 015018 (2014).
[21] N. Sandberg and G. Grimvall, Phys. Rev. B **63**, 184109 (2001).
[22] B. Cheng and M. Ceriotti, Phys. Rev. B **97**, 054102 (2018).
[23] H. M. Gilder and D. Lazarus, Phys. Rev. B **11**, 4916 (1975).
[24] J. N. Mundy, S. J. Rothman, N. Q. Lam, H. A. Hoff, and L. J. Nowicki, Phys. Rev. B **18**, 6566 (1978).
[25] U. Köhler and C. Herzig, Philos. Mag. A **58**, 769 (1988).
[26] G. Neumann and V. Tölle, Philos. Mag. A **61**, 563 (1990).
[27] A. Satta, F. Willaime, and S. de Gironcoli, Phys. Rev. B **60**, 7001 (1999).
[28] B. Grabowski, L. Ismer, T. Hickel, and J. Neugebauer, Phys. Rev. B **79**, 134106 (2009).
[29] J. Pelleg, Philos. Mag. **29**, 383 (1974).
[30] J. N. Mundy, H. A. Hoff, J. Pelleg, S. J. Rothman, L. J. Nowicki, and F. A. Schmidt, Phys. Rev. B **24**, 658 (1981).
[31] R. E. Einziger, J. N. Mundy, and H. A. Hoff, Phys. Rev. B **17**, 440 (1978).
[32] K. Maier, H. Mehrer, and G. Rein, Z. Metallkd. **70**, 271 (1979).
[33] H. Mehrer, J. Nucl. Mater. **69**, 38 (1978).
[34] J. N. Mundy, S. T. Ockers, and L. C. Smedskjaer, Philos. Mag. A **56**, 851 (1987).
[35] R. Bauer, in *Materials Science Forum*, Vol. 15 (Trans Tech Publications, Zurich, 1987), pp. 397–402.
[36] G. Neumann, C. Tuijn, G. De Vries, and H. Bakker, Phys. Status Solidi B **149**, 483 (1988).
[37] R. W. Siegel, *Defects in Metals*, Tech. Rep. (Argonne National Laboratory, Lemont, IL, 1982).
[38] J. Y. Park, H. C. W. Huang, R. W. Siegel, and R. W. Balluffi, Philos. Mag. A **48**, 397 (1983).
[39] K. Eftaxias and V. Hadjicontis, Philos. Mag. Lett. **58**, 69 (1988).

[40] M. I. Mendelev, T. L. Underwood, and G. J. Ackland, J. Chem. Phys. **145**, 154102 (2016).
[41] B. Beeler, Y. Zhang, M. Okuniewski, and C. Deo, J. Nucl. Mater. **508**, 181 (2018).
[42] D. G. Sangiovanni, O. Hellman, B. Alling, and I. A. Abrikosov, Phys. Rev. B **93**, 094305 (2016).
[43] S. M. Foiles, Phys. Rev. B **49**, 14930 (1994).
[44] M. García Ortega, S. Ramos de Debiaggi, and A. Monti, Phys. Status Solidi B **234**, 506 (2002).
[45] M. De Koning, S. Ramos de Debiaggi, and A. Monti, in *Defect Diffus. Forum*, Vol. 224 (Trans Tech Publications, Zurich, 2004), pp. 59–74.
[46] A. Minashin and V. Ryabov, J. Nucl. Mater. **233**, 996 (1996).
[47] L. Bukonte, T. Ahlgren, and K. Heinola, J. Appl. Phys. **115**, 123504 (2014).
[48] I. Novoselov, A. Yanilkin, A. Shapeev, and E. Podryabinkin, Comput. Mater. Sci. **164**, 46 (2019).
[49] M. I. Mendelev and B. S. Bokstein, Philos. Mag. **90**, 637 (2010).
[50] M. I. Mendelev and Y. Mishin, Phys. Rev. B **80**, 144111 (2009).
[51] B. Zhang, AIP Adv. **4**, 017128 (2014).
[52] H. Wen, P.-W. Ma, and C. H. Woo, J. Nucl. Mater. **440**, 428 (2013).
[53] D. Gambino and B. Alling, Phys. Rev. B **98**, 064105 (2018).
[54] Y. Lysogorskiy, T. Hammerschmidt, J. Janssen, J. Neugebauer, and R. Drautz, Modell. Simul. Mater. Sci. Eng. **27**, 025007 (2019).
[55] T. S. van Erp and P. G. Bolhuis, J. Comput. Phys. **205**, 157 (2005).
[56] M. W. Finnis and J. E. Sinclair, Philos. Mag. A **50**, 45 (1984).
[57] G. J. Ackland and R. Thetford, Philos. Mag. A **56**, 15 (1987).
[58] B.-J. Lee, M. I. Baskes, H. Kim, and Y. K. Cho, Phys. Rev. B **64**, 184102 (2001).
[59] X. W. Zhou, R. A. Johnson, and H. N. G. Wadley, Phys. Rev. B **69**, 144113 (2004).
[60] M. Mrovec, D. Nguyen-Manh, D. G. Pettifor, and V. Vitek, Phys. Rev. B **69**, 094115 (2004).
[61] P. M. Derlet, D. Nguyen-Manh, and S. L. Dudarev, Phys. Rev. B **76**, 054107 (2007).
[62] M. Čák, T. Hammerschmidt, J. Rogal, V. Vitek, and R. Drautz, J. Phys.: Condens. Matter **26**, 195501 (2014).
[63] H. Park, M. R. Fellinger, T. J. Lenosky, W. W. Tipton, D. R. Trinkle, S. P. Rudin, C. Woodward, J. W. Wilkins, and R. G. Hennig, Phys. Rev. B **85**, 214121 (2012).
[64] C. Chen, Z. Deng, R. Tran, H. Tang, I.-H. Chu, and S. P. Ong, Phys. Rev. Mater. **1**, 043603 (2017).
[65] W.-X. Song and S.-J. Zhao, J. Mater. Res. **28**, 1155 (2013).
[66] D. E. Smirnova, A. Y. Kuksin, S. V. Starikov, V. V. Stegailov, Z. Insepov, J. Rest, and A. M. Yacout, Modell. Simul. Mater. Sci. Eng. **21**, 035011 (2013).
[67] J.-S. Kim, D. Seol, J. Ji, H.-S. Jang, Y. Kim, and B.-J. Lee, Calphad **59**, 131 (2017).
[68] L. Lang, K. Yang, Z. Tian, H. Deng, F. Gao, W. Hu, and Y.-f. Mo, Modell. Simul. Mater. Sci. Eng. **27**, 045009 (2019).
[69] M. Finnis, *Interatomic Forces in Condensed Matter*, Vol. 1 (Oxford University Press, Oxford, 2003).
[70] M. S. Daw and M. I. Baskes, Phys. Rev. B **29**, 6443 (1984).
[71] M. I. Baskes, Phys. Rev. B **46**, 2727 (1992).
[72] Y. Mishin, M. J. Mehl, and D. A. Papaconstantopoulos, Acta Mater. **53**, 4029 (2005).
[73] S. Plimpton, J. Comput. Phys. **117**, 1 (1995).
[74] G. Kresse and J. Furthmüller, Phys. Rev. B **54**, 11169 (1996).
[75] J. P. Perdew, K. Burke, and M. Ernzerhof, Phys. Rev. Lett. **77**, 3865 (1996).
[76] J. W. Edwards, R. Speiser, and H. L. Johnston, J. Appl. Phys. **22**, 424 (1951).
[77] L. Brewer, Lawrence Berkeley Laboratory Report No. LBL-3720 (1977).
[78] J. M. Dickinson and P. E. Armstrong, J. Appl. Phys. **38**, 602 (1967).
[79] D. Errandonea, B. Schwager, R. Ditz, C. Gessmann, R. Boehler, and M. Ross, Phys. Rev. B **63**, 132104 (2001).
[80] F. Ercolessi and J. B. Adams, Europhys. Lett. **26**, 583 (1994).
[81] P. Brommer and F. Gähler, Modell. Simul. Mater. Sci. Eng. **15**, 295 (2007).
[82] P. Brommer, A. Kiselev, D. Schopf, P. Beck, J. Roth, and H.-R. Trebin, Modell. Simul. Mater. Sci. Eng. **23**, 074002 (2015).
[83] S. V. Starikov and V. V. Stegailov, Phys. Rev. B **80**, 220104(R) (2009).
[84] S. Ryu and W. Cai, Modell. Simul. Mater. Sci. Eng. **16**, 085005 (2008).
[85] A. P. Miiller and A. Cezairliyan, Int. J. Thermophys. **6**, 695 (1985).
[86] I.-K. Suh, H. Ohta, and Y. Waseda, J. Mater. Sci. **23**, 757 (1988).
[87] A. Togo and I. Tanaka, Scr. Mater. **108**, 1 (2015).
[88] B. M. Powell, P. Martel, and A. D. B. Woods, Phys. Rev. **171**, 727 (1968).
[89] J. M. Sanchez and D. De Fontaine, Le Journal de Physique Colloques **38**, C7 (1977).
[90] D. G. Sangiovanni, J. Klarbring, D. Smirnova, N. V. Skripnyak, D. Gambino, M. Mrovec, S. I. Simak, and I. A. Abrikosov, Phys. Rev. Lett. **123**, 105501 (2019).
[91] K. Maier, M. Peo, B. Saile, H. E. Schaefer, and A. Seeger, Philos. Mag. A **40**, 701 (1979).
[92] I. A. Schwirtlich and H. Schultz, Philos. Mag. A **42**, 601 (1980).
[93] M. Suezawa and H. Kimura, Philos. Mag. **28**, 901 (1973).
[94] K. Yamakawa, H. Kugler, and H. Schultz, Radiat. Eff. **105**, 171 (1988).
[95] D. Nguyen-Manh, S. L. Dudarev, and A. P. Horsfield, J. Nucl. Mater. **367**, 257 (2007).
[96] T. R. Armstrong, H. A. Filius, A. Van Veen, and J. R. Heringa, J. Nucl. Mater. **203**, 189 (1993).
[97] P. Söderlind, L. H. Yang, J. A. Moriarty, and J. M. Wills, Phys. Rev. B **61**, 2579 (2000).
[98] B. Meyer and M. Fähnle, Phys. Rev. B **56**, 13595 (1997).
[99] L. Ventelon, F. Willaime, C.-C. Fu, M. Heran, and I. Ginoux, J. Nucl. Mater. **425**, 16 (2012).
[100] G. Henkelman and H. Jónsson, J. Chem. Phys. **113**, 9978 (2000).
[101] Y. Mishin, M. R. Sørensen, and A. F. Voter, Philos. Mag. A **81**, 2591 (2001).
[102] M. W. D. Cooper, S. T. Murphy, and D. A. Andersson, J. Nucl. Mater. **504**, 251 (2018).
[103] S. Starikov and M. Korneva, J. Nucl. Mater. **510**, 373 (2018).
[104] V. Gairola, P. D. Semalty, and P. N. Ram, Pramana **80**, 1041 (2013).

[105] H. Eyring, J. Chem. Phys. **3**, 107 (1935).
[106] G. H. Vineyard, J. Phys. Chem. Solids **3**, 121 (1957).
[107] J. Koettgen, T. Zacherle, S. Grieshammer, and M. Martin, Phys. Chem. Chem. Phys. **19**, 9957 (2017).
[108] L. Zhao, R. Najafabadi, and D. J. Srolovitz, Modell. Simul. Mater. Sci. Eng. **1**, 539 (1993).
[109] A. S. Bochkarev, S. O. Zamulko, O. I. Gorbatov, S. I. Sidorenko, P. Puschnig, and A. V. Ruban, Europhys. Lett. **116**, 16001 (2016).
[110] S. T. Reeve and A. Strachan, Modell. Simul. Mater. Sci. Eng. **27**, 044002 (2019).
[111] A. S. Bochkarev, A. van Roekeghem, S. Mossa, and N. Mingo, Phys. Rev. Mater. **3**, 093803 (2019).
[112] C. Dellago, P. G. Bolhuis, and P. L. Geissler, Adv. Chem. Phys. **123**, 1 (2002).
[113] C. Dellago, P. G. Bolhuis, F. S. Csajka, and D. Chandler, J. Comput. Phys. **108**, 1964 (1998).
[114] P. G. Bolhuis and W. Lechner, J. Stat. Phys **145**, 841 (2011).
[115] A. M. Ferrenberg and R. H. Swendsen, Phys. Rev. Lett. **63**, 1195 (1989).
[116] T. S. van Erp, Phy. Rev. Lett. **98**, 268301 (2007).
[117] P. G. Bolhuis, J. Chem. Phys. **129**, 114108 (2008).
[118] P. N. Kenny and P. T. Heald, Philos. Mag. **29**, 1137 (1974).
[119] R. H. J. Fastenau, L. M. Caspers, and A. Van Veen, Phys. Status Solidi A **34**, 277 (1976).
[120] S. L. Dudarev, Annu. Rev. Mater. Res. **43**, 35 (2013).
[121] S. V. Starikov, Z. Insepov, J. Rest, A. Y. Kuksin, G. E. Norman, V. V. Stegailov, and A. V. Yanilkin, Phys. Rev. B **84**, 104109 (2011).
[122] L. Pavlinov and V. Bykov, Fiz. Metal. i Metalloved. **18**, 459 (1964).
[123] M. Bronfin, S. Bokshtein, and A. Zhukhovitsky, Zavod. Lab **26**, 828 (1960).
[124] W. Danneberg and E. Krautz, Z. Naturforsch. A **16**, 854 (1961).
[125] T. V. Borisov, P. L. Gruzin, L. V. Pavlinov, and G. B. Fedorov, Metal. Pure Metal Sci. **1**, 213 (1959).
[126] A. Choudhury and C. Brooks, Int. J. Thermophys. **5**, 403 (1984).